p-ISSN : 2335-1357 e-ISSN : 2437-1122

Mediterranean Journal of Modeling and Simulation

Med. J. Model. Simul. 10 (2018) 029-044

Optimal Design of Multi-phases Permanent-Magnet Synchronous Machines Using Genetic Algorithms

D. Ouamara [a] [b] *, F. Dubas [a] , S.A. Randi [c] , M.N. Benallal [b] , C. Espanet [d]

[a] Département ENERGIE, FEMTO-ST, CNRS, Univ. Bourgogne Franche-Comté, F90000 Belfort, France

[b] Laboratoire de l'énergie et des systèmes intelligents, Université de Khemis Miliana, Route de Théniet El-Had, 44225, Khemis Miliana, Algérie

[c] Institut VEDECOM, Versailles, France

[d] Univ. Bourgogne Franche-Comté, F90000 Belfort, France

ARTICLE INFO

Article history :
Received May 2018
Accepted August 2018

Keywords :
Genetic algorithm ;
Muli-phases ;
Numerical ;
Permanent-magnet ;
Optimization.

ABSTRACT

In order to design multi-phases permanent-magnet (PM) synchronous machines (PMSMs), a simplified analytical method is used to calculate the various geometrical parameters. The winding of the machines is concentric with two layers and the PMs are mounted on the rotor surface. The sizing model is coupled to an optimization process based on genetic algorithm (AG). The Pareto front obtained from the optimization, made it possible to choose the optimal solution. The optimal variables are injected into the model to calculate the different parameters. The optimization results are then used for two-dimensional (2-D) finite-element simulation, where a power balance is established for each multi-phases PMSMs.

1. Introduction

1.0.1. Context of this paper

In the design of electrical machines, the use of optimization coupled with an analytical model is often used as a solution. The set of variables governing the machine are estimated by an analytical calculation, and according to certain constraints, the algorithm minimizes the objective function that corresponds to the optimal solution. The AGs enable the resolution of multi-objective optimization problems. The advantage is obtaining several optimal solutions in the form of a Pareto front. The choice of the final solution is a compromise between the various optimization criteria [1]-[2].

The PMSMs are characterized by their rotor magnetic field, which is constant. The

*Email : daoud.ouamara@gmail.com

PMs at the rotor produce a high magnetic field in the air-gap, allowing a high-power density. Thus, the PMSMs are very efficient and require less cooling due to the absence of the rotor winding [3]. The chosen winding is concentric with two layers. This type of winding is characterized by low Joule losses at the end-coil, since these are short. The coils can be machined separately from the stator and inserted without contact with the other coils. This makes it possible to achieve interesting values for the copper filling factor in the slots and an automation of the manufacturing process [4].

In addition to the advantages associated with the structure, the multi-phases system ensures the operation in degraded mode [5]. Continuity of service during a fault is the factor that allows multi-phases machines to be attractive in electric traction, as well as the splitting of power (low power per phase) that allows for more robust power electronics components and cheaper. Increasing the phase number allow obtaining a low ripple torque, so decrease the acoustic noise [6].

1.1. Objective of this paper

Optimal design will be performed for four multi-phases PMSMs with two layers concentric winding. The four stator windings are generated from "ANFRACTUS Tool 1.0" developed by [7]. The winding factor of each spatial harmonic is calculated for each structure by the method proposed by [8], and the number of poles is synthesized from the results of the winding factor. Finally, the multi-phases PMSMs studied are :

- **M-5A :** 5-phases/20-slots/16-poles ;
- **M-5B :** 5-phases/20-slots/18-poles ;
- **M-7A :** 7-phases/28-slots/24-poles ;
- **M-7B :** 7-phases/28-slots/26-poles.

The analytical model is described in Section 2, where simplifying assumptions are introduced. Section 3 deals with optimization based on GAs. The requirement specifications, constraints and optimization variables are given. The last section deals with finite-element modeling of the four multi-phases PMSMs. An energy balance is established for each machine studied.

2. Analytical Model Description

2.1. Assumptions

The 2D analytical model of multi-phases PMSMs is based on the following assumptions :

- the magnetic field in the air-gap is assumed to be purely radial ;
- the PMs magnetization is considered purely radial ;
- the PMs are isotropic and have a linear B(H) characteristic (i.e ; constant relative permeability of PMs) ;
- the rotor and stator iron are supposed linear ;
- the saturation effect is taken into account by an optimization constraint ;
- the leakage magnetic flux are neglected ;
- the electrical conductivity is assumed to be zero in all materials (i.e., eddy-currents are neglected) ;
- the armature reaction is negligible compared to the no-load operation.

2.2. Geometrical Model

The main geometric parameters are given in Fig. 1. This figure allows the writing of elementary equations describing the geometry and also the volume and mass of the machine. To illustrate, we give the following examples :

$$R_{si} = R_e + h_{is} + h_d \tag{1}$$

$$m_{sy} = m_{vr}\left({R_{se}}^2 - {R_{si}}^2\right)\pi l_m k_f \tag{2}$$

with m_{sy}y is the mass of stator yoke, m_{vr} the volumetric mass density of iron, l_m the machine length, and k_f the staking factor.

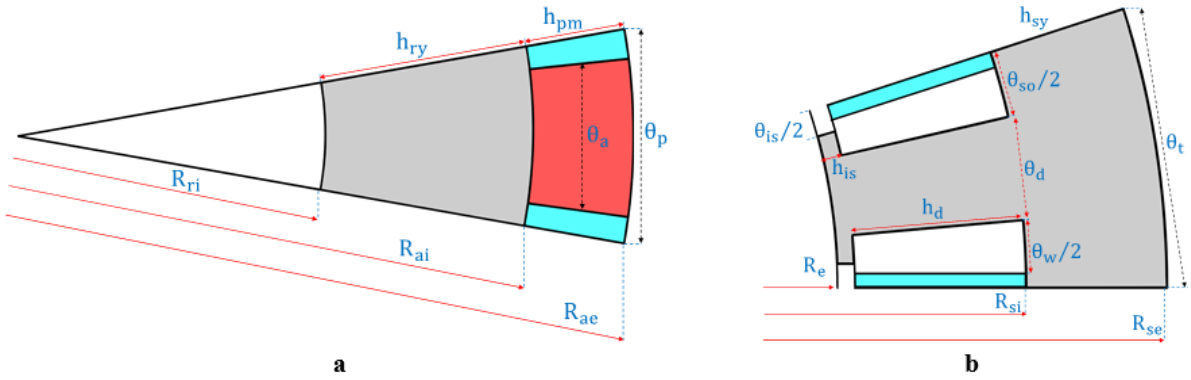

Fig. 1 – Geometry of surface-mounted internal rotor PMSM : (a) rotor and (b) stator

2.3. Magnetic Model

To describe the magnetic operation of the PMSM, we will transform the actual structure into a simplified equivalent structure. The introduction of the Carter coefficient K_c allows this transformation, where the toothed stator and the real air-gap g are replaced respectively by a slotless stator and a fictitious air-gap $g^{'}$. This usual transformation is illustrated in Fig. 2. However, the PMs presence increases artificially the real air-gap g of the machine into an effective air-gap g_e, the latter is defined by [9] :

$$g_e = g + \frac{h_a}{\mu_{ra}} \tag{3}$$

The Carter coefficient K_c is defined by [10] :

$$K_c = \frac{b_{od}}{b_{od} - K_\gamma g_e} \tag{4}$$

with $b_{od} = \theta_{is} \cdot R_e$ the width of the isthmus-opening, and K_γ the coefficient of slot width which is expressed by :

$$K_\gamma = \frac{4}{\pi}\left[\frac{b_{is}}{2g_e} arct\left(\frac{b_{is}}{2g_e}\right) - ln\sqrt{1 + \left(\frac{b_{is}}{2g_e}\right)^2}\right] \tag{5}$$

where b_{is} the width of the isthmus-opening.

Finally the fictitious air-gap $g^{'}$ and the corrected stator radius $R_e^{'}$ are respectively given by :

$$g' = g + (K_c - 1)\, g_e \tag{6}$$

$$R_e^{'} = R_e + (K_c - 1)\, g_e \tag{7}$$

The magnetic equivalent circuit as shown by Fig. 3 can model the slotless structure. The resolution of the magnetic equivalent circuit allows the magnetic flux density determination in the air-gap B_g.

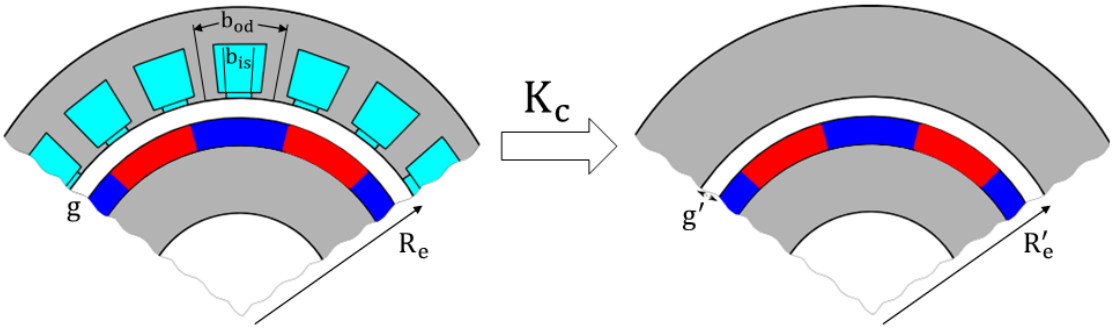

Fig. 2 – Transformation of a toothed stator into a slotless stator by applying Carter coefficient K_c

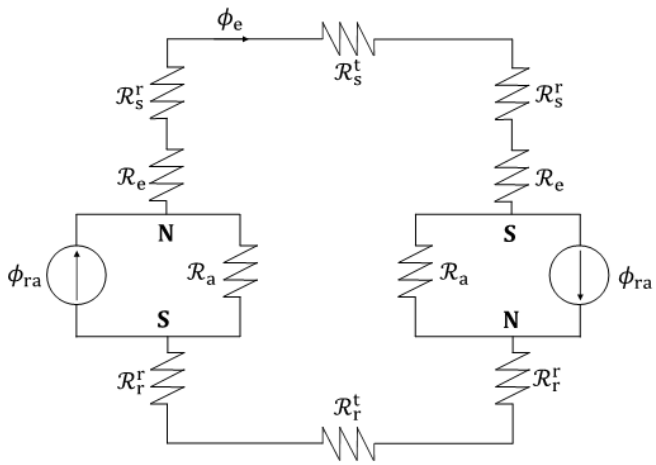

Fig. 3 – Magnetic equivalent circuit associated to the slotless structure for 2-poles

Assuming that the iron permeability is sufficiently large in front of the air-gap and PMs permeability, the iron reluctances (i.e., R_s for the stator and R_r for the rotor) will be small compared to air-gap and PMs reluctances (i.e., R_e for the air-gap and R_a for the PMs). In this case, the iron reluctances are considered as a disturbance only of the air-gap reluctance, it can be eliminated by introducing a reluctance factor k_r. The latter is a constant slightly greater than 1 ($1 \leq k_r \leq 1.2$) which increases the air-gap reluctance to compensate the omission of the iron reluctance [11]. The magnetic flux in the air-gap

ϕ_e can be expressed using the division of the magnetic flux (i.e., as the current divider in an electric equivalent circuit), and we will have :

$$\phi_e = \frac{1}{1 + k_r \frac{\mathcal{R}_e}{\mathcal{R}_a}} \phi_{ra} \tag{8}$$

with $\phi_{ra} = B_{ra} \cdot S_a$ where B_{ra} represents the remanent flux density of the PMs and S_a the passage area of the magnetic flux in the PMs.

Using the general expressions of the air-gap and PMs reluctances as well as the flux concentration C_ϕ,

$$\mathcal{R}_g = \frac{g'}{\mu_0 S_g{}'} \tag{9}$$

$$\mathcal{R}_a = \frac{h_a}{\mu_0 \mu_{ra} S_a} \tag{10}$$

$$C_\phi = \frac{S_a}{S_g{}'} \tag{11}$$

the magnetic flux density in the air-gap can be written in the following form :

$$B_e = \frac{\phi_e}{S_g{}'} = \frac{C_\phi}{1 + k_r C_\phi \frac{e'}{h_a}} B_{ra} \tag{12}$$

where h_a is the thickness of the PMs, and g' & S'_a are respectively the length and the passage area of the magnetic flux in the air-gap corrected by the Carter coefficient K_c.

The expressions of the maximum magnetic flux density respectively in the tooth, the isthmus, the stator yoke and the rotor yoke are given by :

$$B_d = \frac{\phi_d}{l_d l_m k_f} \tag{13}$$

$$B_{is} = \frac{\phi_d}{l_{is} l_m k_f} \tag{14}$$

$$B_{sy} = \frac{\phi_{sy}}{h_{cs} l_m k_f} \tag{15}$$

$$B_{ry} = \frac{\phi_{ry}}{h_{cr} l_m k_f} \tag{16}$$

where l_d is the width of the tooth; l_{is} the width of tooth-tips; h_{cs} & h_{cr} respectively the thickness of the stator and rotor yoke; and ϕ_d, ϕ_{sy} & ϕ_{ry} respectively the maximum magnetic flux in the stator teeth, stator and rotor yoke which are defined by :

$$\phi_d = \theta_t B_e \; R_e{}' l_m \tag{17}$$

$$\phi_{sy} = \phi_{ry} = \phi_e/2 \tag{18}$$

According to Boucherot's theorem, the RMS value of the fundamental back electromotive force (EMF) is given by [12] :

$$E_1 = K_e\Omega \text{ with } K_e = \frac{1}{\sqrt{2}}\xi_{wh} p n_s R_e{}' l_m B_{e_1} \text{ and } B_{e_1} = \frac{4}{\pi} cos\left[(1-\alpha_a)\frac{\pi}{2}\right] B_e \tag{19}$$

where Ω the rotational angular speed of the rotor, n_s the turns number, ξ_{wh} the winding factor calculated from the connection matrix, α_a the PM pole-arc to pole-pitch, and $h = p$ the synchronous harmonic whose p is the number of pole pairs.

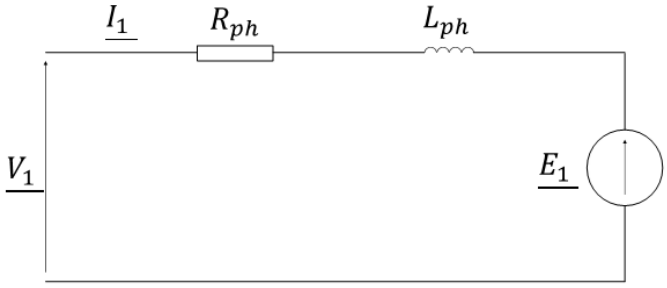

Fig. 4 – Single-phase equivalent diagram of the unsaturated PMSM with smooth-poles

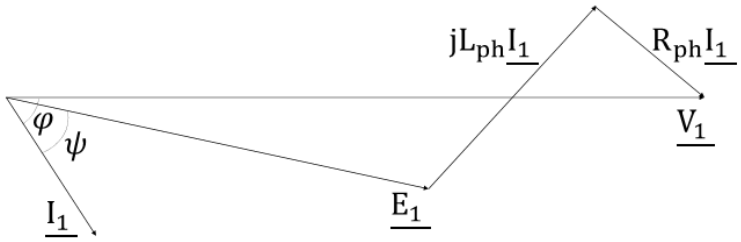

Fig. 5 – Bhen-Eschenburg's diagram of unsaturated PMSM with smooth-poles

2.4. Electrical Model

The equations describing electrical operation are based on the classical unsaturated and smooth-poles PMSM model as shown in Fig. 4. The associated Bhen-Eschenburg's diagram is represented on the Fig. 5. The electrical resistance of a phase for the concentric winding is given by [13] :

$$R_{ph}(T_c) = \rho_c(T_c)\frac{l_{coil}}{S_c} n_s n_{coil} \tag{20}$$

with ρ_c the electrical resistivity of the copper at T_c, S_c the section of a conductor, l_{coil} the length of a coil, and $n_{coil} = (Q_s L_y)/2m$ the number of coils per phase where Q_s, L_y and m are respectively the number of slots, layers and phases.

The magnetic inductance of a phase can be expressed by [14] :

$$L_{ph} = p\mu_0 \frac{n_s^2 l_m l_d}{g' + h_a} \tag{21}$$

Therefore, the magnetic reactance of a phase is defined by :

$$X_{ph} = L_{ph} p\Omega \tag{22}$$

The RMS value of the fundamental current I_1 is fixed by the electromagnetic torque T, viz.,

$$I_1 = \frac{T}{mK_e \cos(\psi)} \tag{23}$$

with ψ the phase shift between fundamental current and fundamental back EMF.

According to Fig. 5, the RMS value of the fundamental phase to neutral voltage V_1 is defined by :

$$V_1 = \sqrt{(E_1 \cos(\psi) + R_{ph} I_1)^2 + (E_1 \sin(\psi) + X_{ph} I_1)^2} \tag{24}$$

2.5. Power Balance

In this section, we will describe the different stator and rotor losses. It should be noted that the mechanical losses will be neglected. The Joule losses will be calculated via the classic Ohm relationship. The iron losses include the eddy-current and hysteresis losses. It should be noted that the excess losses in the magnetic circuit are assumed negligible and are not treated.

2.5.1. Copper Losses

In sinusoidal steady state, the Joule losses of the m-phases are given by :

$$p_J = m R_{ph} I_1^2 \tag{25}$$

2.5.2. Iron Losses

The iron losses in PMSMs are localized in the magnetic circuit and more precisely to the stator. The rotor iron losses will be neglected because the variations of the magnetic flux density created by the stator currents in the rotor yoke are very small compared to those of PMs. The stator iron losses can be expressed by [10] :

$$p_{iron} = p_{ed} + p_{hys} \tag{26}$$

$$p_{ed} = K_{ed} (p\Omega)^2 B_{max}^2 m_{sta} \tag{27}$$

$$p_{hys} = K_{hys} p\Omega B_{max}^2 m_{sta} \tag{28}$$

where B_{max} is the peak value of the magnetic flux density in the iron core; m_{sta} the mass of stator iron; and K_{ed} & K_{hys} are respectively the coefficients of the eddy-currents and hysteresis. How to calculate these coefficients is given in Section 4.3.

2.5.3. Magnet Losses

The PM eddy-current losses without the slotting effect can be estimated in the same way as iron eddy-current losses according to [15] :

$$p_{PM} = \frac{V_{PM} h_a^2 B_{yr}^2 (p\Omega)^2}{12\rho_{PM}} \tag{29}$$

where V_{PM} and ρ_{PM} are respectively the volume and the electrical resistivity of PMs.

2.6. Efficiency

Finally, the efficiency of the PMSMs is defined by :

$$\eta = \frac{P_{em}}{P_{em} + p_J + p_{iron} + p_{PM}} \tag{30}$$

where $P_{out} \cong P_{em} = T \cdot \Omega$ is the electromagnetic power equivalent to the output power P_{out}.

2.7. Thermal Model

The thermal behavior of the PMSM is modeled in a basic way. We consider that the convection at the stator outer surface. For a convection coefficient $h_{conv} = 15W/((m^2K))$, the average temperature rise δT of the stator and winding is expressed by :

$$\delta T = \frac{p_J + p_{iron}}{2\pi R_{se} l_m h_{conv}} \tag{31}$$

3. Multi-Objective Optimization

The AG used, allowing the optimal design of electrical machines [16], is NSAGAII type (Non-Dominated Sorting Genetic Algorithm II) [17]. The analytical model is coupled with this algorithm to obtain the optimal parameters according to the variables and imposed constraints.

3.1. Problem Optimization

The requirements specification are given in Table. 1, where electromagnetic performances of electric machines are imposed. Note that the requirement specifications are the same for the four PMSMs studied.

In our study, the chromosomes of the AG represented the sizing parameters of the PMSM. The variation ranges of these parameters are reported to the Table. 2. Optimization constraints are applied to magnetic flux density in the air-gap, the stator yoke and teeth, as well as in the machine length and the electromagnetic torque. These constraints are reported to the Table. 3. The objective function consists in minimizing the total mass of PMSMs, while maximizing the efficiency. In mathematical terms, our multi-objective optimization problem can be formulated by :

$$\begin{cases} \min f(x) = [f_1(x),\ 1/f_2(x)] \\ \textit{under constraint} \\ x \in C \end{cases} \tag{32}$$

where $f_1(x)$ & $f_2(x)$ are respectively the objective functions of the total mass and efficiency, x the vector of optimization variables, and C the constraints set of equality, inequality and explicit bounds with $C = \{g(x) \leq 0$, et $x^L \leq x \leq x^U\}$.

3.2. Optimizations Results

The Pareto fronts obtained, representing the mass/efficiency solutions, are shown in Fig. 6. The efficiency is proportional to the mass, so the choice of the optimal machine is a dilemma between high efficiency and low mass. After choosing the optimal solution, the values of the associated optimization variables to chosen solution are automatically injected into the model to estimate the geometrics parameters of multi-phases PMSMs.

Given that, Pareto fronts are very close, and for performing an electromagnetic comparison for the same volume. We unify the geometric parameters for all the machines studied. The characteristics of the machines optimized are reported in Table. 4.

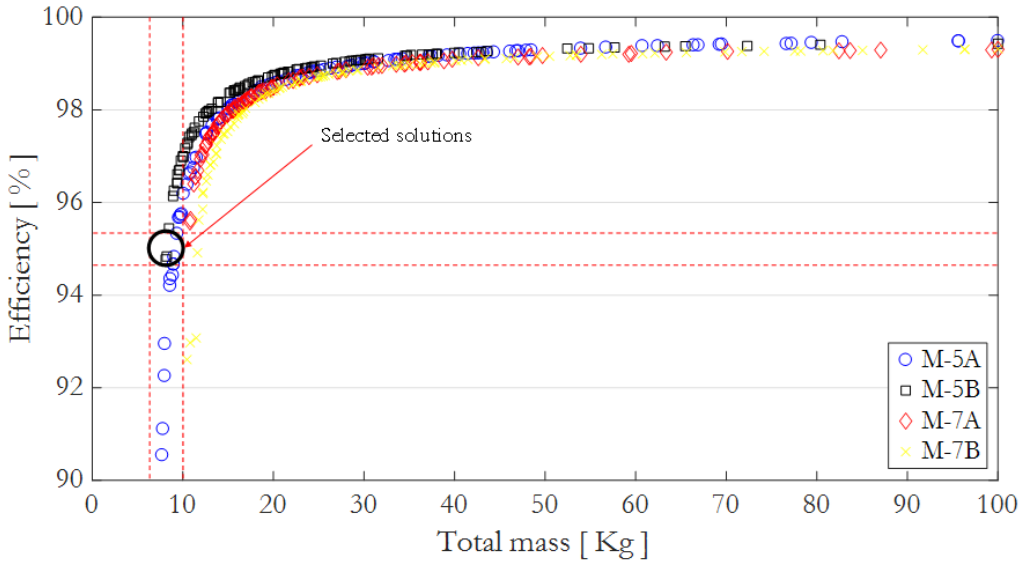

Fig. 6 – Pareto fronts : mass/efficiency

Table 1 – Requirements specification

Designation	**Symbol**	**Value**	**Unit**
Torque	T	30	Nm
Electromagnetic power	P_{em}	9.42	kW
Rotational speed	N	3,000	rpm
External diameter	D_{es}	$\leq$150	mm
Machine length	l_m	$\leq$150	mm

Table 2 – Variation ranges of optimization parameters

Designation	**Symbol**	**Range**	**Unit**
Slot-opening/tooth-pitch	α_{so}	[30,70]	%
Isthmus-opening/slot	α_{is}	[30,70]	%
PM pole-arc/pole-pitch	α_a	[70,100]	%
Winding-opening/slot	α_w	[90,95]	%
Rotor internal radius	R_{ri}	[10,50]	mm
Rotor yoke height	h_{cr}	[10,50]	mm
PM height	h_a	[10,50]	mm
Air-gap length	g	[0.5,1.5]	mm
Tooth height	h_d	[10,50]	mm
Stator yoke height	h_{cs}	[10,50]	mm
Machine length	l_m	[10,150]	mm
Diameter of copper wires	d_{cu}	[0.2,2]	mm
Turns number	n_s	[1,500]	-

Table 3 – Optimization constraints

Designation	**Symbol**	**Range**	**Unit**
Electromagnetic torque	T	[/- 30]	Nm
Air-gap magnetic flux density	B_e	[0.6-1.1]	T
Stator yoke magnetic flux density	B_{cs}	[0.8-2]	T
Stator tooth magnetic flux density	B_d	[0.8-2]	T

Table 4 – Characteristic data of the optimized machines

Designation	**Symbol**	**M-5A**	**M-5B**	**M-7A**	**M-7B**	**Unit**
Slots number	Q_s	20	20	28	28	-
Phases number	m	5	5	7	7	-
Poles number	$2p$	16	18	24	26	-
Slot-opening/tooth-pitch	α_{so}	60				%
Isthmus-opening/slot	α_{is}	53				%
PM pole-arc/pole-pitch	α_a	72				%
Winding-opening/slot	α_w	92				%
Stator diameter at the air-gap surface	D_e	49.4				mm
External diameter	D_{es}	65.7				mm
Internal diameter	D_i	34.9				mm
Stator yoke height	h_{cs}	3				mm
Rotor yoke height	h_{cr}	3				mm
PM height	h_a	2.5				mm
PM mass	m_{PM}	0.179				kg
Tooth height	h_d	4.8				mm
Machine length	l_m	100				mm

4. 2-D Numerical Simulation

4.1. Introduction

The 2-D numerical simulations are carried out in transient magnetic. For the studied PMSMs, the magnetic steel M270-35A of Arcelor Mittal has been considered. The PMs type is NdFeB whose remanent flux density is equal to 1.1 T at 100°C. No-load/Load simulations will determine the back EMF, the electromagnetic torque as well as the torque ripple, and the iron/copper/PMs losses.

4.2. No-load Simulation

The back EMF waveform of the phase A of each PMSM at 3,000 rpm and its harmonic spectrum are given by the Fig. 7. The back EMF of the 5-phases PMSMs has a higher amplitude compared to the 7-phases PMSMs.

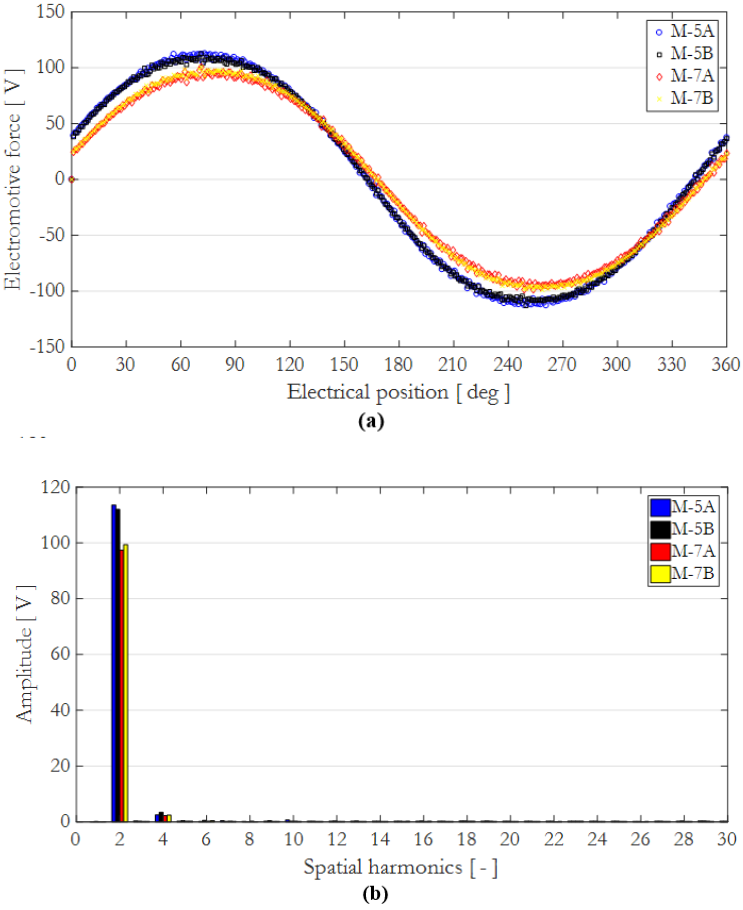

Fig. 7 – Back EMF : (a) Waveform and (b) Harmonic spectrum

4.3. Load Simulation

The distribution map of the magnetic flux densities for the four PMSMs, as well as the maximum value of magnetic flux density at each region are shown in Fig. 8. The saturation level of 5-phases PMSMs is very similar in different regions, and also for 7-phases PMSMs. However, the magnetic flux density of 7-phases PMSMs are relatively weak in comparison with the magnetic flux density of 5-phases PMSMs. This is due to the lower number of

turns in 7-phases PMSMs.

Fig. 9 shows the electromagnetic torque and torque ripple for the four PMSMs. Considering weakness of torque ripple, the cogging torque is neglected. The mean value of electromagnetic torque is 30 Nm, what satisfy the requirements specification. From Fig. 9, we observe the decrease of the torque ripple by increasing the phases number. Noting that the M-5A and M-7A machines have the same type of winding, and the M-5B and M-7B machines have another type of winding.

The DC copper losses (i.e., without the skin effect) in the windings at I=30 A are 90 W for 5-phases PMSMs, and 108 W for 7-phases PMSMs. The increase of the phases number causes additional losses.

The PMs eddy-current losses with the slotting effect for the four PMSMs are illustrated in Fig. 10. These losses in 7-phases PMSMs are lower than 5-phases PMSMs because of number of turns per phase. This is necessary in order to make the comparison for the same torque equal to 30 Nm. Making the same number of turns per phase for the four PMSMs will involve a higher electromagnetic torque for 7-phases PMSMs, so high magnetic flux densities in the different regions and so the geometrical dimensions must be increased. In this case, the comparison will lose its physical meaning.

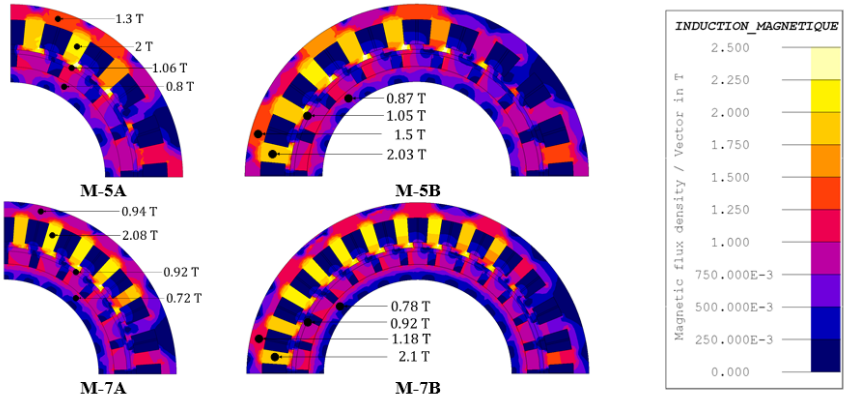

Fig. 8 – Distribution map of magnetic flux densities for the PMSMs

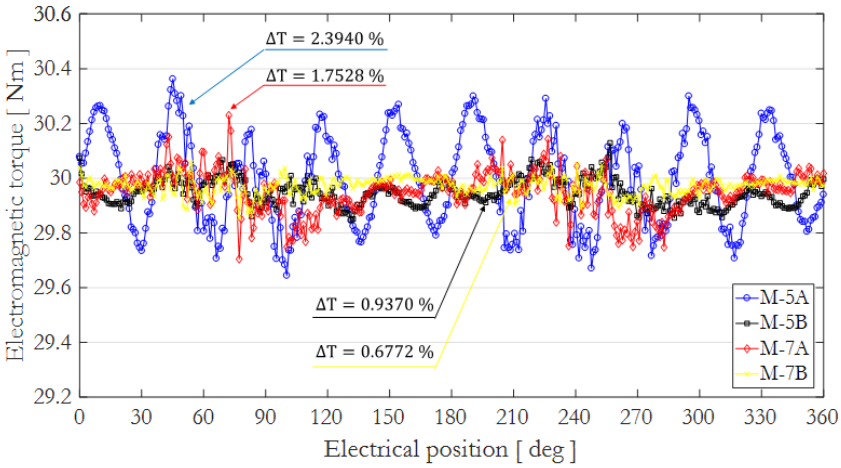

Fig. 9 – Electromagnetic torque

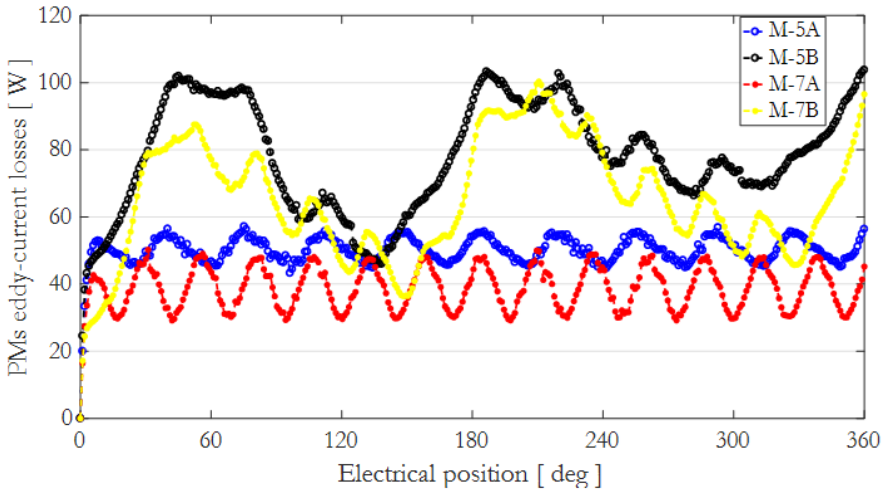

Fig. 10 – PMs eddy-current losses

The iron losses are separated on three types of losses : i) hysteresis, ii) eddy-current, and iii) excess. Those magnetic losses are determined numerically from Bertotti's method [18] and with using "Loss Surface" (LS) module [19], noting that (LS) module is include in Flux 2D. Various losses per volume, defined by Bertotti's method, are given by :

$$dP_{hys} = K_{hys}\ {B_{max}}^2\ f \text{ (Hysteresis)} \tag{33}$$

$$dP_{ed} = \frac{\pi^2\ \sigma\ d^2}{6}\ (B_{max}\ f)^2 \text{ (Eddy-current)} \tag{34}$$

$$dP_{ex} = 8,67.\ K_{ex}\ (B_{max}\ f)^2 \text{ (Excess)} \tag{35}$$

The coefficients K_{hys} and K_{ex} are determined from the sheet loss curves (W/kg) for each frequency, given by the manufacturer. The general equation interpolating these curves of losses for sheet M270-35A is given by [20] :

$$W_{sp} = \frac{1}{\rho}\ \left[120\ {B_{max}}^2\ f + 0.4\ (B_{max}f)^2 + 6.4(B_{max}f)^{3/2}\right] \tag{36}$$

By taking two levels of magnetic flux density in the PMSM and replacing them in the previous equation, we will have two equations with two unknowns that will allow us to obtain the values from K_{hys} and K_{ex}.

The physical parameters and the coefficients are given in Table 5 for M270-35A sheet. Fig. 11 represents the iron losses with Bertotti's method [see Fig. 11(a)] and LS module [see Fig. 11(b)]. As that the iron losses are linked to magnetic flux density and to frequency, it is clear that the PMSM whose frequency is high will have more losses than other machines. Results of this study are summarized in Table 6.

Table 5 – Data of the sheet M270-35A (Bertotti's Method)

Designation	**Symbols**	**M-5A**	**M-5B**	**M-7A**	**M-7B**
Volumetric mass density	ρ	7,650 kg.m^{-3}			
Electrical conductivity	σ	1.92 $\times$ 10^{6} S.m^{-1}			
Thickness	d	0.35 mm			
Hysteresis coefficient	K_{hys}	125.296	125.937	127.868	128.489
Excess coefficient	K_{ex}	0.738	0.738	0.738	0.738

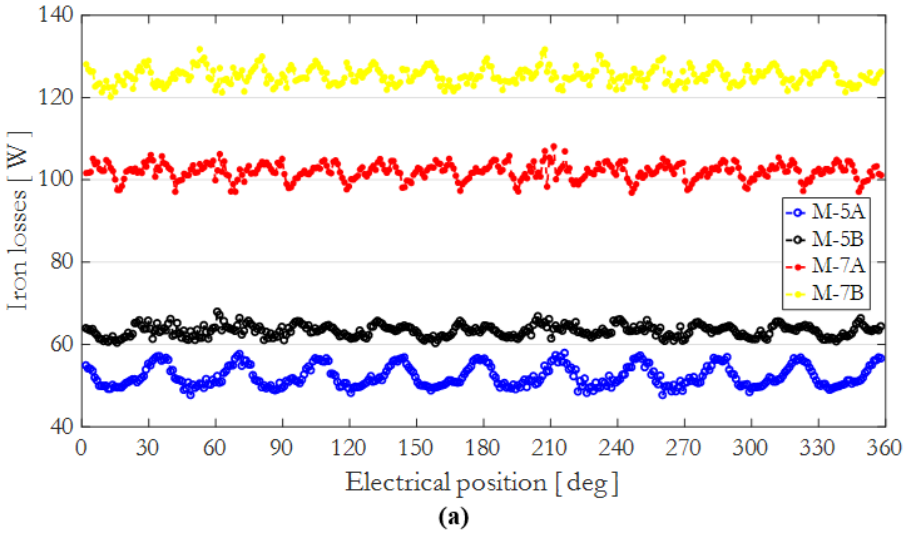

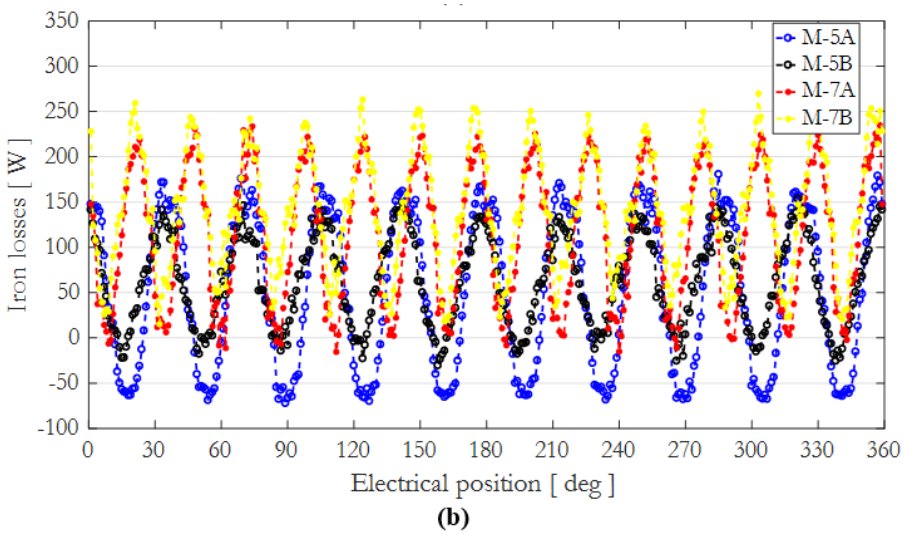

Fig. 11 – Iron losses : (a) Bertotti's method, and (b) LS module

Table 6 – Summary of the comparison

	M-5A	**M-5B**	**M-7A**	**M-7B**
Slots number	20	20	28	28
Phases number	5	5	7	7
Poles number	16	18	24	26
Winding	Concentrated all teeth wound (two layers)			
Bore diameter	49.4 mm			
Outside diameter	65.7 mm			
Iron length	100 mm			
Total volume	0.22 L			
Rotation speed	3,000 rpm			
Electromagnetic torque	30 Nm			
Output power	9.42 kW			
Turns/phase number	20	20	14	14
Torque ripple	2.3940 %	0.9370 %	1.7528 %	0.6772 %
DC copper losses	90 W	90 W	108 W	108 W
PMs eddy-current losses	50.1 W	77.8 W	38.7 W	65.3 W
Iron losses (LS)	54.2 W	61.4 W	109.5 W	142.5 W
Iron losses (Bertotti)	52.8 W	64.1 W	102.5 W	125.9 W

5. Conclusion

The purpose of this work is to propose a simple but consistent sizing model. The model makes it possible to have all the required geometrical parameters in a few seconds (saving time), while respecting the electromagnetic constraints. The results of the 2-D finite-elements allowed the validation of the solution obtained for the four PMSMs. The approach of the model can be applied to other topologies of electrical machines, by adding and/or removing some of the equations constituting it.

REFERENCES

[1] X. Roboam, "Integrated Design by Optimization of Elecrical Energy Systems," John Wiley & Sons, Inc, ISBN 978-1-84821-389-0, 2012, Chapter 2, pp. 45-103.

[2] R. Benlamine, F. Dubas, S.A. Randi, D. Lhotellier, and C. Espanet, "Design by optimization of an axial-flux permanent-magnet synchronous motor using genetic algorithms," in Proc. ICEMS, Busan, South Korea, 26-29 Oct., 2013.

[3] C. Chan and K. Chau, "An overview of power electronics in electric vehicles," IEEE Trans. Ind. Elec., vol. 44, no. 1, pp. 3–13, Feb. 1997.

[4] A. Soualmi, F. Dubas, A. Randria, and C. Espanet, "Comparative study of permanent-magnet synchronous machines with concentrated windings for railway application," in Proc. ICEMS, Beijing, China, 20-23 Aug., 2011.

[5] F. Scuiller, J-F. Charpentier, E. Semail et S. Clénet "Comparison of two 5-phase Permanent Magnet machine winding configurations. Application on naval propulsion specifications," in Proc. IEMDC, Antalya, Turkey, 03-05 May, 2007.

[6] D. Ouamara, F. Dubas, M.N. Benallal, S.A. Randi, and C. Espanet, "Electromagnetic Comparison of 3-, 5-, and 7-phases Permanent- Magnet Synchronous Machines : Mild

Hybrid Traction Application," Mediterranean Journal of Modeling & Simulation, vol. 06, no. 01, pp. 12-22, Sep. 2016.

[7] D. Ouamara, F. Dubas, M.N. Benallal, S.A. Randi, and C. Espanet, "Automatic Winding Generation using Matrix Representation - ANFRACTUS TOOL 1.0," Acta Polytechnica, vol. 58, p. 37, Feb 2018.

[8] D. Ouamara, F. Dubas, S.A. Randi , M.N. Benallal, and C. Espanet, "General Calculation of Winding Factor for Multi-Phase/-Layer Electrical Machines Irrespective of Poles Number," COMPEL, Under review.

[9] F. Dubas and C. Espanet, "Exact analytical model of the no-load flux density in the air-gap, permanent magnets and the rotor yoke for the surface mounted permanent magnet motors," International Review of Electrical Engineering, vol. 2, no. 3, pp. 425-437, May-Jun. 2007.

[10] F. Dubas, "Conception d'un moteur rapide à aimants permanents pour l'entrainement de compresseurs de piles à combustible," Ph.D dissertation, Electrical Engineering and systems (LEES), University of Franche-Comté (UFC), Belfort, France, 2006.

[11] D. Hanselman, "Brushless Permanent Magnet Motor Design," Magna Physics Publishing, 2003

[12] G. Séguier and F. Notelet, "Electrotechnique industrielle," Lavoisier, 3rd edition, 2006.

[13] C. Espanet, A. Miraoui, and J.M. Kauffmann, "Optimal design of an high torque DC brushless in-wheel motor," in Proc. IEMDC, Madison, WI, USA,01-04 Jun., 2003.

[14] H.C.M. Mai, F. Charih, F. Dubas, D. Chamagne, and C. Espanet, "Comparaison de deux bobinages pour la propulsion d'un véhicule hybride urbain," European Journal of Electrical Engineering, vol. 14, no. 2-3, pp. 255-285, Jun. 2011.

[15] H. Jussila, "Concentrated winding multiphase permanent magnet machine design and electromagnetic properties - case axial flux machine," Ph.D dissertation, University of Lapeenranta, 2009.

[16] L. Belguerras, and L. Hadjout, "Multi-objective Design Optimization of Slotless PM Motors Using Genetic Algorithms Based on Analytical Field Calculation," Computational Methods for the Innovative Design of Electrical Devices, vol. 327, pp. 19-37, 2011.

[17] K. Deb, A. Pratap, S. Agarwal, and T. Meyarivan, "A fast and elitist multiobjective genetic algorithm : NSGA-II," IEEE Trans. Evol. Comp., vol. 6, no. 2, pp. 182-197, Aug. 2002.

[18] G. Bertotti, "General properties of power losses in soft ferromagnetic materials," IEEE Trans. Magn., vol. 24, no. 1, pp. 621-630, Jan. 1988.

[19] T. Chevalier, A. Kedous-Lebouc, B. Cornut, and C. Cester, "A new dynamic hysteresis model for electrical steel sheet," Physica B : Condensed Matter, vol. 275, no. 1-3, pp. 197-201, Jan. 2000.

[20] R. Wrobel, P.H. Mellor, and D. Holliday, "Thermal modeling of a segmented stator winding design," IEEE Trans. Ind. Appl., vol. 47, no. 5, pp. 2023-2030, Sep./Oct. 2011.